

High-velocity moving groups in the Solar neighborhood in Gaia DR2

Baluev, R. V., Shaidulin, V. Sh., and Veselova, A. V.

Saint Petersburg State University, 7–9 Universitetskaya Emb., St Petersburg 199034,
Russia
e-mail: r.baluev@spbu.ru*Received March 02, 2020*

ABSTRACT

We use an improved wavelet analysis technique to reconstruct the (U, V, W) velocity distribution for ~ 250000 stars from Gaia DR2, residing in the solar neighborhood of 200 pc. The 2D wavelet transforms for three bivariate distributions (U, V) , (U, W) , and (V, W) were investigated. Though most of currently known (low-velocity) stellar moving groups are densely overlapped in these diagrams, our analysis allowed to detect and disentangle about twenty statistically significant 3D groups of stars with high velocities. Most of them appear new. We also discuss the issue of correct noise thresholding in the wavelet transform and highlight the importance of using a global rather than local statistic for that. Using of a local significance measure may lead to an overstated statistical confidence for individual patterns due to the effect of multiple testing.

Key words: *Moving groups, Milky Way kinematics, Gaia DR2, Solar neighborhood, statistical wavelet analysis.*

1. Introduction

Stellar moving groups in the solar neighbourhood have been studied for a long time. In the 20th century a detailed study was performed by Olin Eggen starting in the 1960s (e.g. Eggen, 1965, 1996), in particular, he investigated the structure of the Sirius and Hyades moving groups (Eggen, 1960a,b). The Hyades group itself along with the Ursa Major group has been known since the 19th century (see Proctor, 1869) according to data on alignment of the velocities of several stars. Over the 20th and 21st centuries a variety of stellar streams and moving groups including Tucana–Horologium, β Pictoris, TW Hydrae, AB Doradus and other have been discovered and investigated (see reviews in Torres et al. 2008; Gagné et al. 2018; Lee and Song 2019).

A variety of methods was created for detection of moving groups and classification of individual stars into groups. A series of algorithms BANYAN I (Malo et al., 2013), BANYAN II (Gagné et al., 2014), BANYAN Σ (Gagné et al., 2018)

as well as LACEwING (Riedel et al., 2017) take into account not only the space velocities UVW, but also the Galactic coordinates XYZ. Complex algorithms also include constraints based on distances and colors/magnitudes.

In a number of studies a detailed analysis of structures on the $U-V$ plane was carried out. Michtchenko et al. (2018) proposed that the stellar moving groups in the solar neighborhood could be explained by the spiral arms perturbations. Authors proposed that Coma-Berenices and Hyades-Pleiades groups are located inside of the corotation radius and the Sirius group is related to several overlapping outer Lindblad resonances. Monari et al. (2019) analyzed the ridge-like structures in local velocity space and discussed structures that could be formed by the resonances of the large bar of the Galaxy. Authors showed that several ridges can be related to resonances with the bar and two of them can be associated with the Hercules moving group in local part of velocity space.

Ramos et al. (2018) performed a decomposition of the distribution of approximately 5 million stars in the V_R-V_ϕ plane with the wavelet transformation in a number of regions near the Sun. Authors found several long structures on the V_R-V_ϕ plane with approximately constant azimuthal velocity. Several structures follow lines of nearly constant energy and resemble the Sirius group. Hyades or Hercules probably follow lines of nearly constant angular momentum. Such different dynamical characteristics may indicate different origins of the structures: Sirius stream may be related to phase-mixing processes, but Hyades/Hercules may be formed as a resonant structure due to perturbation of bar and/or the spiral arms. Authors also observed several candidates moving groups and some of them are not related to already known groups.

The additional criteria such as the photometrical data or chemical composition are used to determine the membership probabilities for stars. Cochrane and Smith (2019) compiled samples of late-type dwarf stars for twelve moving groups and analyzed the loci of ensembles of stars on two-color diagram (a $(FUV-B)$ color index plotted against $(B-V)$). Authors found the relationship between the photometric index based on $(FUV-B)$ color and the ages of late-type dwarf stars. They suppose that addition of FUV photometry would be useful for membership determination of late-F, G, and K dwarf stars.

Lee and Song (2018, 2019) created models for nearby stellar young moving groups and presented lists of confirmed members and model parameters of groups. Authors emphasized the difference of membership probabilities from BANYAN series of methods; for example, according to (Lee and Song, 2019) HR 8799 belongs to the β Pictoris moving group, but in other studies this star is considered as a member of Columba group.

It is important to note the discussion of the status of stellar groups within 100 pc by Mamajek (2015). Author stated that the Ursa Major, Hyades, Coma Ber and η Cha groups are real star clusters and their stellar densities exceed the density of the local part of Galactic disc, the association TW Hya was called a

well-characterized group of approximately 3 dozen stars, and the Tuc-Hor group could be an ensemble of several subgroups. The Columba, Carina, 32 Ori groups and χ^1 For cluster were reported to be the likely physical groups. Mamajek stated that the Argus, Oct-Near, Her-Lyr, Castor, IC 2391 Supercluster are unlikely physical groups; Her-Lyr, Castor and IC 2391 may probably be considered as streams.

As we can see, many stellar moving groups are already known in the literature. They are summarized below in Appendix A. However, this is an ongoing discussion still containing multiple controversies and ambiguities. In this work we undertake an attempt to perform a systematic search for *statistical* moving groups in the UVW-space, based on the Gaia DR2 (Gaia Collaboration; Brown et al., 2018; Gaia Collaboration; Katz et al., 2018). We intend to use the statistical wavelet analysis algorithm presented initially in (Baluev, 2018) for univariate (1D) distributions and recently extended to the bivariate (2D) analysis (Baluev et al., 2020). This method has certain improvements in comparison with wavelet analysis previously used by other authors (Skuljan et al., 1999; Romeo et al., 2008; Bobylev et al., 2010; Bobylev and Bajkova, 2016; Bajkova and Bobylev, 2018; Ramos et al., 2018). In particular, it has an important accent on the correct determination of statistical significance. In fact, this work also represents a new field-test for this 2D algorithm, in addition to the asteroid families search made by Baluev and Rodionov (2020).

The structure of the paper is as follows. In Section 2. we describe how our statistical samples are constructed based on the Gaia data. In Section 3. we describe several points of our wavelet analysis algorithm and discuss some conventions related to the formal criteria behind a statistical cluster or a group. In Section 4. we present our main results of the analysis.

2. Data samples

We exported a portion of Gaia DR2 from *Vizier* database, containing stars with known radial velocities. This resulted in more than 7 million records. Then stars with parallax lower than 5 mas (those outside the heliocentric radius of 200 pc) were removed. Inside this solar neighborhood stars with big relative parallax uncertainties (greater than 20%) were also removed. This left 352000 records. Then the transformation to galactic velocities U , V , W was performed using procedure described in *Gaia Data Release 2 Documentation* (<https://gea.esac.esa.int/archive/documentation/GDR2/>).

Briefly, for each star we can compute local basis:

$$\mathbf{p} = \begin{bmatrix} -\sin \alpha \\ \cos \alpha \\ 0 \end{bmatrix}, \quad \mathbf{q} = \begin{bmatrix} -\cos \alpha \sin \delta \\ -\sin \alpha \sin \delta \\ \cos \delta \end{bmatrix}, \quad \mathbf{r} = \begin{bmatrix} \cos \alpha \cos \delta \\ \sin \alpha \cos \delta \\ \sin \delta \end{bmatrix}, \quad (1)$$

where α , δ are the right ascension and declination, respectively. Then velocity is

$$\mathbf{v} = \frac{\kappa}{\varpi} \mu_\alpha^* \mathbf{p} + \frac{\kappa}{\varpi} \mu_\delta \mathbf{q} + v_r \mathbf{r}. \quad (2)$$

Here $\kappa = 4.740470446$ expresses the astronomical unit in km yr s^{-1} , ϖ is parallax, μ_α^* is proper motion in right ascension with $\cos \delta$ factor, μ_δ is proper motion in declination, v_r is radial velocity. We can obtain galactic velocities by rotation of velocity \mathbf{v} to galactic frame with orthogonal matrix A :

$$\begin{bmatrix} U \\ V \\ W \end{bmatrix} = A \mathbf{v}, \quad (3)$$

$$A = \begin{bmatrix} -0.0548755604162154 & -0.8734370902348850 & -0.4838350155487132 \\ +0.4941094278755837 & -0.4448296299600112 & +0.7469822444972189 \\ -0.8676661490190047 & -0.1980763734312015 & +0.4559837761750669 \end{bmatrix}.$$

Finally, we removed the stars with too big velocity uncertainties greater than 3 km s^{-1} . For that purpose we calculated a velocity covariance matrix for each star, using the uncertainties provided by Gaia DR2. We apply the so-called delta method. First, the velocity Jacobian is

$$J = \frac{\partial \mathbf{v}}{\partial \mathbf{u}} = \left[\frac{\partial \mathbf{v}}{\partial \alpha}, \frac{\partial \mathbf{v}}{\partial \delta}, \frac{\partial \mathbf{v}}{\partial \varpi}, \frac{\partial \mathbf{v}}{\partial \mu_\alpha^*}, \frac{\partial \mathbf{v}}{\partial \mu_\delta}, \frac{\partial \mathbf{v}}{\partial v_r} \right], \quad \mathbf{u} = [\alpha, \delta, \varpi, \mu_\alpha^*, \mu_\delta, v_r]^T \quad (4)$$

and it is a 3×6 matrix. Here,

$$\begin{aligned} \frac{\partial \mathbf{v}}{\partial \alpha} &= \frac{\kappa}{\varpi} \mu_\alpha^* \frac{\partial \mathbf{p}}{\partial \alpha} + \frac{\kappa}{\varpi} \mu_\delta \frac{\partial \mathbf{q}}{\partial \alpha} + v_r \frac{\partial \mathbf{r}}{\partial \alpha}, & \frac{\partial \mathbf{v}}{\partial \delta} &= \frac{\kappa}{\varpi} \mu_\delta \frac{\partial \mathbf{q}}{\partial \delta} + v_r \frac{\partial \mathbf{r}}{\partial \delta}, \\ \frac{\partial \mathbf{v}}{\partial \varpi} &= -\frac{\kappa}{\varpi^2} \mu_\alpha^* \mathbf{p} - \frac{\kappa}{\varpi^2} \mu_\delta \mathbf{q}, & \frac{\partial \mathbf{v}}{\partial \mu_\alpha^*} &= \frac{\kappa}{\varpi} \mathbf{p}, & \frac{\partial \mathbf{v}}{\partial \mu_\delta} &= \frac{\kappa}{\varpi} \mathbf{q}, & \frac{\partial \mathbf{v}}{\partial v_r} &= \mathbf{r}, \\ \frac{\partial \mathbf{p}}{\partial \alpha} &= \begin{bmatrix} -\cos \alpha \\ -\sin \alpha \\ 0 \end{bmatrix}, & \frac{\partial \mathbf{q}}{\partial \alpha} &= \begin{bmatrix} \sin \alpha \sin \delta \\ -\cos \alpha \sin \delta \\ 0 \end{bmatrix}, & \frac{\partial \mathbf{r}}{\partial \alpha} &= \begin{bmatrix} -\sin \alpha \cos \delta \\ \cos \alpha \cos \delta \\ 0 \end{bmatrix}, \\ \frac{\partial \mathbf{q}}{\partial \delta} &= \begin{bmatrix} -\cos \alpha \cos \delta \\ -\sin \alpha \cos \delta \\ -\sin \delta \end{bmatrix}, & \frac{\partial \mathbf{r}}{\partial \delta} &= \begin{bmatrix} -\cos \alpha \sin \delta \\ -\sin \alpha \sin \delta \\ \cos \delta \end{bmatrix}. \end{aligned} \quad (5)$$

The small difference of the velocity \mathbf{v} is expressed through a linear approximation as

$$\Delta \mathbf{v} = J \Delta \mathbf{u}. \quad (6)$$

Then the 3×3 variance-covariance matrix is approximated as

$$\text{Var}(\mathbf{v}) = \mathbb{E} \Delta \mathbf{v} \Delta \mathbf{v}^T \simeq J \text{Var}(\mathbf{u}) J^T. \quad (7)$$

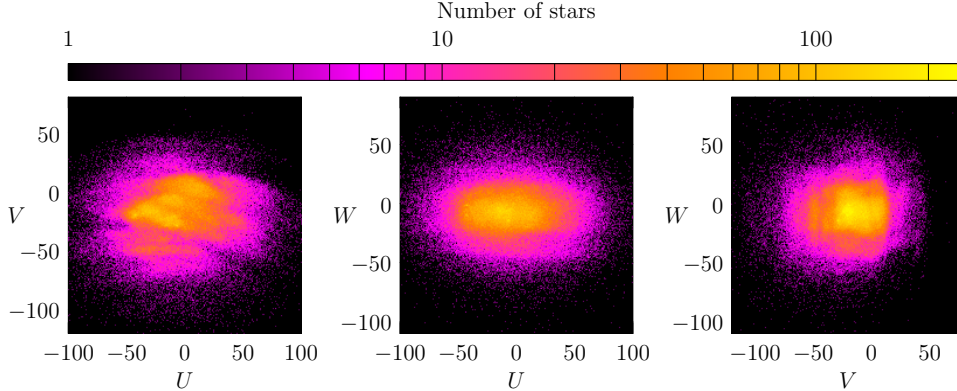


Fig. 1. Three bivariate velocity distributions: UV -plane, UW -plane, VW -plane (from left to right, respectively).

The matrix $\text{Var}(\mathbf{v})$ defines an ellipsoid in \mathbb{R}^3 , and we adopt its semi-major axis σ_v (or the largest matrix eigenvalue) as an indicative characteristic of the velocity uncertainty.

Our primary sample contains only stars with $\sigma_v < 3 \text{ km s}^{-1}$. Fig. 1 shows three 2D histograms of this sample. Its size is $N = 245499$ sources. We also considered a smaller subsample with the uncertainty limit below 1 km s^{-1} which resulted in only $N = 45879$ sources.

We also considered additional indicators available in Gaia DR2 that could be helpful in removing unreliable sources from our samples. In particular, we investigated the so-called excess astrometric noise of a source, ε_i . This is an additional error term added quadratically to the observational uncertainties. Mathematically, it is analogous to the ‘jitter’ known well in radial velocity surveys (Wright, 2005; Baluev, 2009). It appears if the empiric scatter of observation is significantly larger than their expected uncertainties. Multiple reasons can cause such a disagreement, e.g. (i) additional noise sources, or (ii) various model inaccuracies. In the first case, this ε_i is already taken into account in our σ_v through the uncertainties in \mathbf{u} . The effect of ε_i decreases in such a case as $1/\sqrt{N_{\text{obs}}}$, where N_{obs} is number of observations of a source. The second case indicates some systematic errors of the astrometric model, and one its possible cause is the presence of an unseen companion (astrometric binary). In such a case its effect would not decrease as $1/\sqrt{N_{\text{obs}}}$, because it is not a random quantity. Given that, the uncertainties of \mathbf{u} may appear understated as they implicitly imply such a factor through astrometric model fitting. Hence, the values of ϖ and μ might then appear distorted more than expected, and so would the derived UVW components. We therefore decided to roughly estimate the effect of ε_i for each source, under the assumption that it is a systematic error rather than random noise.

This can be done as follows. Given the formula (2), the astrometric part of the spatial velocity vector is $\kappa\mu/\varpi$. In this treatment the ‘jitter’ ε_i represents some characteristic systematic bias of each observation. Such a bias may distort either

the parallax ϖ , resulting in a velocity error $\sim \kappa \varepsilon_i \mu / \varpi^2$, or the proper motion μ , generating a error of $\sim \kappa \varepsilon_i / (\varpi T)$, where T is the observation time span. Combining these quantities into a sum-of-squares metric, we obtain

$$\delta v_{\text{sys}} \sim \frac{\kappa \varepsilon_i}{\varpi} \sqrt{\frac{1}{T^2} + \left(\frac{\mu}{\varpi}\right)^2}. \quad (8)$$

This quantity can be used as a measure of possible systematic errors that may appear e.g. because of unclassified astrometric companions of a source. We computed δv_{sys} for each object in our samples, and filtered out those that had it above 3 km/s (or 1 km/s, respectively). Setting $T = 5$ yr, we found just about 80 such sources in the larger sample, and only 1 in the smaller one. These potentially problematic sources were spread over the UVW space without clear concentration, so they are unlikely to affect our statistical analysis, even if their spatial velocity is inaccurate.

3. Wavelet analysis and treatment of statistical clusters

We are going to use the wavelet analysis method described in (Baluev, 2018) and (Baluev et al., 2020). It is based on the continuous wavelet transform (CWT):

$$Y(a, b) = \int_{\mathbb{R}^n} f(x) \psi\left(\frac{x-b}{a}\right) dx, \quad (9)$$

where $f(x)$ is the probability density function (PDF) under study, $n = 1$ or $n = 2$ is the dimension of the task (of the random variable x and of the shift parameter b). The scale parameter a is always a scalar quantity, and $\psi(t)$ is an analysing wavelet. The wavelet is assumed to be radially symmetric for $n = 2$, so it is actually a function of just the length of its argument vector.

The analysis algorithm involves the following stages:

1. Estimation of the CWT (9) based on the input random sample.
2. Computing the associated noise thresholding (or goodness-of-fit) statistic relative to some comparison (null) model.
3. Construction of the most economic (in terms of the number of wavelet coefficients) PDF model based on the iterative CWT inversion, until all deviations decrease below the noise thresholds.

The algorithm involves optimized minimum-noise wavelets and inversion kernels. Also, we emphasize especially that it relies on the extreme value distribution when performing the noise thresholding. This is different from many other works that use, basically, a single value distribution for that goal. We advocate that the latter approach is inadequate for this task, because it ignores the fact that multiple values

of $Y(a, b)$ (multiple wavelet coefficients) are tested simultaneously in a single analysis. In such a case it is necessary to include a statistical correction for the effect of multiple testing: the probability to make a statistical mistake among many values is much larger than for just a single value. Otherwise, the noise thresholds would appear inadequately tight and a lot of noisy wavelet coefficients may be wrongly declared as significant. This issue is broadly analogous to the effect of unknown frequency in the periodogram analysis (Baluev, 2008; Süveges, 2014).

Unfortunately, unjustified neglect of this issue is shared between multiple wavelet analysis works regarding the stellar statistics. In particular, we believe that (Skuljan et al., 1999) and more recently (Ramos et al., 2018) overestimated the number of detectable structures. In the latter work they appeared so numerous that authors decided to reduce their number by joining them into branches, and discarded those that appeared outside of any branch. However, the true underlying issue could be just an overstated significance that appeared due to multiple testing of numerous wavelet coefficients.

However, in this work we would like to make additional focus on the interpretation issue instead of just significance. This is a further development of the ideas presented in the 1D analysis by Baluev and Shaidulin (2018), in particular in what concerns the formal definition of a *statistical cluster*. The last term is not strict: one may adopt quite different criteria of what PDF structures should be attributed to isolated clusters of objects. Although there is no universally applicable formal definition of a cluster, we still need to set up some formalized convention or at least a guide how do we distinguish a cluster from other PDF anomalies, especially in the 2D case.

The wavelet analysis inherently implies such a formalized definition. Let us first note that our algorithm may use a wavelet function of one of the following forms:

$$\Psi(t) = \begin{cases} \varphi'(t) \text{ or } \varphi''(t), & n = 1, \\ \Delta\varphi(t), & n = 2, \end{cases} \quad (10)$$

where $\Delta\varphi$ is the Laplace operator and φ is a ‘generating function’, which represents a bell-like smoothing kernel. This generating function is determined in an optimal way to reduce the noise, and is different for each wavelet, see (Baluev, 2018; Baluev et al., 2020).

The definition (10) implies that $Y(a, b)$ is either a smoothed first or second derivative of $f(x)$, if $n = 1$, or a smoothed Laplacian of $f(x)$, if $n = 2$. In this work, we do not use the case with the first derivative (the WAVE/WAVE2 wavelets), since it usually appeared not so informative regarding practical results. Therefore, the wavelet analysis here implies that our primary objective is either the second derivative $f''(x)$ or the Laplacian $\Delta f(x)$:

$$Y(a, b) = a^2 \int_{\mathbb{R}^n} \Delta f(x) \varphi\left(\frac{x-b}{a}\right) dx \stackrel{a \rightarrow 0}{\sim} a^{n+2} \Delta f(b) \int_{\mathbb{R}^n} \varphi(t) dt. \quad (11)$$

This formula is obtained through integrating (9) by parts.

Hence, the CWT of this type is simply an analogue of the statistical kernel density estimator (KDE), but (i) applied to $\Delta f(x)$ rather than to $f(x)$, and (ii) involving all possible smoothing scales a at once. It is important that $\Delta f(x)$, or just f'' in the 1D case, plays a crucial role here. In fact, the CWT simply estimates them via smoothing.

The particular shape of the smoothing kernel φ was sought from the optimality condition minimizing noise in the CWT estimate. The optimal kernel is different for $n = 1$ and $n = 2$, resulting in the so-called CBHAT and 2DOPT wavelets, respectively (Baluev, 2018; Baluev et al., 2020). Notice that these wavelets have a qualitatively similar shape to the classical MHAT wavelet, but still are quite different. The MHAT wavelet (the second derivative of a Gaussian) is not suitable in tasks of this type because it generates too much non-Gaussian skewed noise in the CWT.

Now let us consider how to define a cluster. The 1D case is illustrated in Fig. 2. We consider a few toy PDF models there, each is a superposition of two Gaussians that model two displaced statistical families of objects. The Gaussians always have the same width (variance) and constant positions, but different relative contribution. The relative contribution of the secondary family varies from $p = 0$ to $p = 0.4$.

One might argue that the PDF should simply be bimodal to ensure that there are two families instead of just one, but it appears that such a requirement is excessively strong. As we can see, the PDF is bimodal only in the most prominent case $p = 0.4$, but the second family still can be easily noticed even if there is no bimodality. In particular, we can see clear hint of an inhomogeneous structure for $p = 0.2$. This appears because the curvature of the graph changes the sign. It suddenly becomes upward-convex at the secondary family (as it was near the primary peak).

This observation suggests that the second derivative f'' provides a good formal criterion of a statistical cluster. Formally, a cluster can be defined as zone where $f''(x)$ is negative. If there is no additional sign changes in f'' , as for $p = 0.05$, then the second family becomes very uncertain. It appears just like a PDF excess that can be interpreted in various alternative ways. This definition of a cluster via the sign changes of f'' is basically a formalized version of the guides presented in (Baluev and Shaidulin, 2018).

The 2D clusters can be determined in a similar way. In this case we consider the Laplacian $\Delta f(x)$ which is estimated by our wavelet analysis via the kernel smoothing. Formally, a 2D cluster can be defined as any disconnected domain where $\Delta f < 0$ (the PDF is convex). Importantly, this core domain would necessarily be surrounded by a counter-signed ‘concavity ridge’. If there is no such a ridge then the domain is not disconnected (not isolated), and the PDF pattern cannot be reliably identified as a cluster.

Unfortunately, even these formal criteria appeared incomplete for our practical goals. They are constructed only for the cases with $n = 1$ or $n = 2$, but in actual-

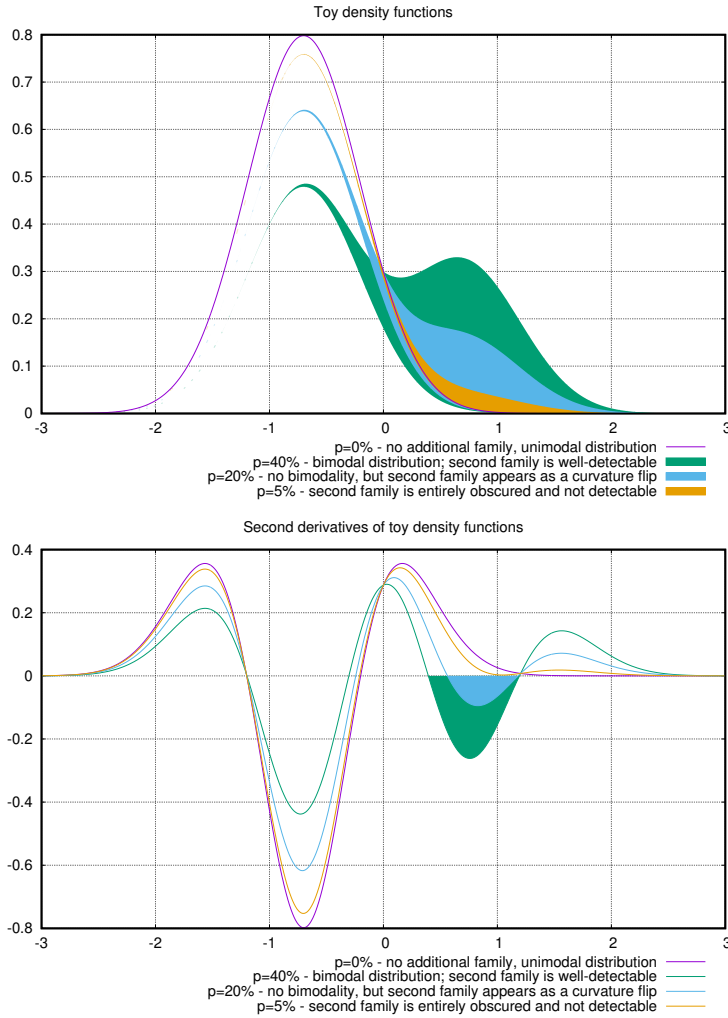


Fig. 2. Illustration of the formalized definition of a statistical cluster (or a group).

ity we deal with at least $n = 3$ parameters (U, V, W). We currently do not have a working 3D wavelet analysis algorithm, because it requires additional theory work related to the noise significance thresholds, and additional computing optimizations. We have to deal with 2D marginalized (projected) PDFs of the 3D velocity distribution. This may reveal useful results too, but our objective criterion of a cluster is then diluted. In particular, the overlapping effect may take place, when two clusters partly merge in some 2D projection, but they can be distinguished in the third dimension. In such conditions we adopt our cluster criteria as a useful guiding, but we treat them more adaptively. For example, we additionally investigate possible substructures within all isolated convexity domains.

4. Disentangling moving groups detected by 2D wavelet analysis

In this work we do not utilize the CWT (9) directly. This appears quite difficult in the 2D case, because the CWT should then be considered as a function in 3D space. Leaving this CWT at intermediate computing stages without detailed interpretation, we finally consider the denoised PDF models reconstructed by our iterative matching pursuit algorithm from the estimated CWT. These models represent the most economic models still in a statistical agreement with the input sample (see details in Baluev et al., 2020).

If some structure appears in such a PDF model then it should necessarily pass the adopted significance threshold in the CWT. In practice, however, the PDF may simultaneously contain multiple structures with quite different magnitude (e.g. statistical clusters of different richness). In particular, small-scale structures usually have smaller magnitude too. And due to the poor contrast, the weaker patterns remain hardly seen in the PDF, even if they are pretty significant in comparison with noise. In (Baluev and Rodionov, 2020) this issue was solved by considering the Laplacian Δf instead of the PDF model f itself. The Laplace operator highlights all smaller-scale structures, so such structures are seen well in $\Delta f(x)$ regardless of the background (which is suppressed). Also, the Laplacian is useful to outline statistical clusters, as described in Sect. 3.

4.1. 1D analysis

We start from analysing 1D distributions for the U , V , and W components of the velocity. The corresponding 1D PDF models obtained for the 2-sigma noise-cleaning level are shown in Fig. 3, together with histograms. Additionally, we also plot the so-called ‘contrasted curvature’ of the PDF, defined as

$$C_1(x) = \sqrt{\frac{-f''(x)}{2f(x)}}. \quad (12)$$

This entity is an f'' -based indicator that (i) additionally highlights structures in the distribution tails, where $f(x)$ is small, and (ii) has the same dimension as $f(x)$, so it can be plotted on the same graph with $f(x)$.¹

We can highlight the following conclusions from the 1D analysis.

1. The 1D PDFs are either unimodal or have rather inconclusive irregular shape (in case of V).
2. Our C_1 indicator reveals several inhomogeneities related to the behaviour of the PDF curvature. Formally, they represent some 1D density concentrations, but of course we do not interpret them further because they likely involve multiple overlapped 2D or 3D structures.

¹This C_1 was derived from the quadratic Taylor decomposition of $f(x)$, namely $1/C_1$ is equal to the abscissa shift δx necessary to reduce $f(x)$ to its local linear gradient.

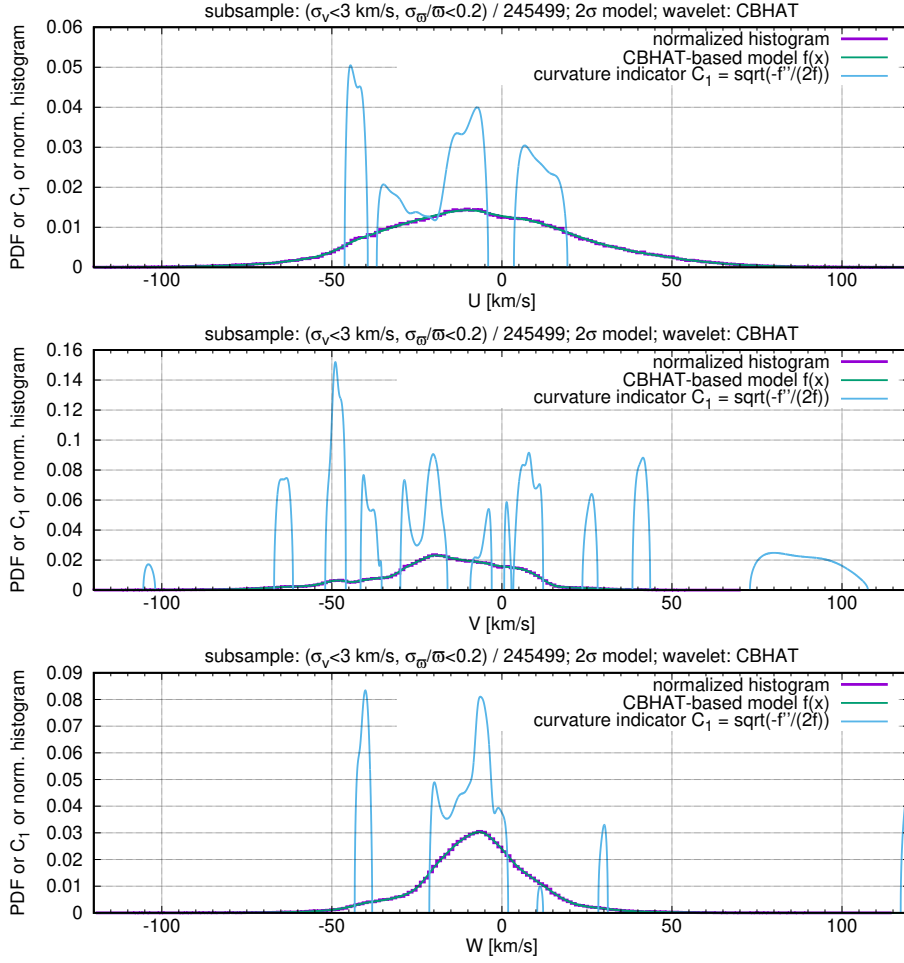


Fig. 3. Three univariate velocity PDFs constructed by the 1D wavelet analysis for the larger sample ($\sigma_v < 3$ km s⁻¹). Histograms normalized by the bin width are shown and almost coincide with the PDF. The PDF curvature indicator C_1 (see text) is also plotted.

3. Three different noise thresholding levels (1,2,3-sigma) resulted in almost the same PDF models (so we showed just the 2-sigma ones). This is expected, because whenever the sample size is so large, the significance threshold becomes very abrupt: a particular structure is either non-significant at all or quickly attains high significance. This contrasts with what was obtained for exoplanetary samples (Baluev and Shaidulin, 2018), because exoplanetary samples were not so rich.
4. Apparently, all three PDF models follow the histograms very closely. One may ask then: is the wavelet analysis indeed necessary here? Could we just stick with simple histograms? Of course, we intentionally plotted such well-fitting histograms for comparison. We could arbitrarily increase the bin

width, losing small-scale details, or decrease it, resulting in an increased noise. Basically, the wavelet analysis adaptively finds some most suitable local smoothing scale thanks to its multiresolution nature. Also, the histogram says nothing reliable about the formal significance of PDF structures.

5. The standalone structure revealed by the C_1 indicator for $V = +75 \dots +110$ km/s is an artifact, because it corresponds to the PDF level of $\sim 10^{-5}$, far in the tail where there is no sample sources. Similar artifacts exist in other 1D distributions (partly seen in the 1D W-plot, and beyond abscissa margins in the U-plot). These false structures are likely analogous to the Gibbs phenomenon from the Fourier analysis (Baluev and Shaidulin, 2018). In this work they are very small in absolute magnitude and easily distinguishable by additional investigation. In 2D distributions they appear as a subtle diffraction-like ring surrounding the entire sample.

The 1D analysis is expectedly inconclusive due to the overlapping effect. We need to consider at least 2D distributions to secure more reliable statistical groups.

4.2. 2D analysis

Now let us proceed to the bivariate distributions. Considering three pairwise combinations (U, V) , (U, W) , and (V, W) , we passed each sample through the 2D analysis pipeline from (Baluev et al., 2020). This resulted in 2D models of the corresponding PDFs. After that, we also computed their Laplacians. This was done using the asymptotic approximation (11) for a small scale a .

After some experimenting with graphs we introduced, by analogy with the curvature indicator C_1 , an additional ‘log-balanced’ curvature indicator C'_2 :

$$C'_2 = \log(1 + \sigma^2 |C_2|) \operatorname{sign} C_2, \quad C_2 = \frac{\Delta f}{2f}. \quad (13)$$

Here $\sigma^2 = \sigma_1^2 + \sigma_2^2$ is the cumulative variance of two variables that we consider, and C_2 is analogous to C_1 . This new quantity C'_2 introduces a mixed linear-logarithmic scale (linear for small C_2 , but logarithmic for large $|C_2|$, preserving its sign). This enables a more clear and contrast visual representation of Δf in a 2D heatmap plot.

Our main results are shown in Fig. 4, Fig. 5, and Fig. 6. We plot the PDF model itself (only for the two-sigma noise threshold), and the corresponding Laplacian indicator C_2 . In the latter case, we also draw a zero-level contour line to outline possible isolated geometric structures, if any. Finally, we also put in these plots all the known moving groups from Appendix A.

In the Laplacians we can see a lot of fine structures, standalone as well as irregular patterns, likely representing partly overlapped configuration. The most rich plots appear for (U, V) and (V, W) variables. Unfortunately, most of these 2D structures involve overlapping effects, even if they appear as isolated at the first view. The overlapping issue was not resolved entirely even in two dimensions,

and it appeared here even more complicated than it was for the asteroid families (Baluev and Rodionov, 2020).

Most of the known moving groups concentrate densely in the central part of the graphs. They all mix into a few big diffuse maxima, so it does not seem there are good chances to disentangle them in our work. The corresponding text labels cannot be resolved in these plots, and to demonstrate the issue even further we give their expanded zooms in Fig. 7 and Fig. 8.

However, there are multiple peripheral PDF concentrations that may be cross-identified in different 2D projections. They represent some new high-velocity moving groups that we may now investigate and characterize.

4.3. *Disentangling standalone 3D moving groups*

We used the same approach to disentangle overlapped families as in (Baluev and Rodionov, 2020). For each isolated domain found in any of our 2D distributions, we cut out the corresponding subsample. The subsample was cut out based on an elliptic mask selected manually to cover the necessary 2D domain. Then for all these subsamples we performed 1D wavelet analysis with respect to the remaining third variable. This enabled us to identify possible overlapped components as 1D clusters located at different levels of the third coordinate. Of course, this analysis did not always allow to perform an unambiguous disentangling. We often faced an irresolvable issues related to too dense overlapping, or overlapping of more than two groups within the same 2D domain, or difficulties due to complicated irregular 3D geometry of the groups.

However, we were able to unambiguously disentangle almost 20 moving groups listed in Table 1. In this table we give an approximate range in each dimension of the UVW-space, and the 2D diagrams where the group appears. The boundaries of each cluster correspond to the domain where $\Delta f < 0$ (in the 2D projection that revealed this group) or from the range where $f'' < 0$ (for dimensions analysed by the 1D algorithm). This means that tails of each group are ignored. Virtually these ranges refer to only kernel portion of a group. For example, if the group is radially symmetric and Gaussian then such a 2D boundary would correspond to $\sqrt{2}$ -sigma deviation, while the 1D-boundary would be the 1-sigma one. However, most of these groups do not look to be either symmetric or Gaussian, and under a close investigation their shape often appears rather complicated. Moreover, boundaries of a small-scale group can be distorted (typically understated) due to a large-scale background PDF curvature (see Fig. 2). In some uncertain cases we had to determine the boundaries rather subjectively, but in general we expect that they correspond to only the central part of each groups, covering very roughly about $\sim 50\%$ of group members.

From the other side, we could identify several famous open clusters (Praesepe, Hyades, Pleiades and AB Doradus), for which our range estimates appear significantly larger than those given in literature. We cannot confirm that narrow ranges

based on our wavelet analysis, though this might be an effect of velocity uncertainty (1 – 3 km/s for the most sources), of the clusters internal structure or some other issue. Notice that e.g. Riedel et al. (2017) and Gagné et al. (2018) provide very different velocity ranges for Hyades. We worked only in the space UVW, so our velocity ranges may possibly include stars that deviate a lot in term of XYZ. This may have an effect of additional velocity spreading.

Apart from those famous clusters, we could presumably identify in this list only the Arcturus stream (Navarro et al., 2004). Other our statistical groups do not have a cross-identification with any of the known moving groups from the Appendix A, so they represent some new ones.

We should also notice that our wavelet algorithm was tuned to detect patterns of near-circular shape, due to the use of radially symmetric wavelets. However, unlike the asteroid families (Baluev and Rodionov, 2020), the stellar moving groups tend to have irregular shape in the velocity space. Some structures in Table 1 appear disproportionally elongated or compressed in a single dimension. They appear statistically significant only when projected onto the compressed axes. However, they would not be detected at all if they did not align so luckily with the coordinate axes. Most probably, such arbitrarily oriented elongated structures also exist, but remained undetected in our analysis.

4.4. *Verifying the statistical reliability of the results*

Let us now try to verify how adequate was our wavelet algorithm in terms of noise thresholding, i.e. does it indeed filter out all (or most) noisy patterns as expected. We use the following approach for that: analyse two similar samples — a big one and a smaller — and compare the results. We consider the analysis to be reliable in view of this criterion, if all patterns revealed in the smaller sample are confirmed by the larger one.

So, in addition to our primary sample, we also processed the smaller subsample with $N \sim 50000$ sources ($\sigma_v < 1 \text{ km s}^{-1}$). These results are presented in Fig. 9 and Fig. 10.

One might expect that the second sample should be capable to reveal finer structures, because it contains more accurate velocities. But in actuality there is no such subtle patterns, while the reduction of sample size increased statistical noise instead, so the number of detectable structures decreased drastically. Nonetheless, we can see five peripheral spots in these graphs indicating some statistically significant PDF convexities. Each of them is confirmed by the larger-sample analysis of Fig. 4–6. Neither of patterns detected in the small sample is disproved by the larger one. Therefore, this suggests additional confirmation that our analysis algorithm does not generate false structures.

Table 1
Disentangled moving groups detected by bivariate wavelet analysis

No.	2D diagrams	U , km/s	V , km/s	W , km/s	comment
1a	UV	+35..+70	+30..+50	-25..+15	might be joined into a single arc-like structure
1b	UV, VW	-40..+30	+20..+50	-40..-20	
2	UV, VW	-40..+0	+20..+34	-5..+20	
3	UV, VW	-65..-40	0..+10	-20..+15	
4a	VW	-45..+25	-35..-10	-45..-30	might be joined into a single structure
4b	VW, UV	-30..+35	-10..+10	-38..-50	
5	VW, UV	-20..+20	0..+10	+10..+25	
6	VW, UV	-20..+20	-10..0	+10..+16	
7	UV, UW	-45..-40	-22..-17	-12..-7	Praesepe cl.
8	UV, UW	-45..-40	-22..-17	-3..+1	Hyades cl.
9	UV, VW	-10..-3	-30..-25	-18..-12	Pleiades cl., AB Doradus
10	VW, UV	-70..-50	-32..-42	-22..-10	
11	VW, UV	-24..-13	-44..-36	-23..-12	
12	VW, UV	+20..+26	-44..-36	-25..-10	
13	UV, VW	-40..+20	-75..-60	-20..+10	
14	UV, VW	-40..+40	-120..-90	-40..+20	Arcturus stream?
15	UV, VW	-4..+24	-40..-16	+5..+15	
16	VW	-50..+60	-80..0	+50..+70	very marginal and uncertain
17	UV, VW	-70..+40	-80..0	-70..-90	very marginal and uncertain

5. Conclusions

Our underlying goal was to assess the applicability and usefulness of the wavelet analysis in the stellar statistics. Although there were multiple interesting results like the list of moving groups above with confirmed statistical significance, this work revealed several important pitfalls.

1. There is a heavy overlapping effect between different stellar groups. In fact, nearly all known moving groups merge so densely in the UVW-space that they form together just a few large-scale maxima. Even though we tried to disentangle several groups in the 3D velocity space UVW, it is still possible that some of them are heterogeneous when viewed in the coordinate space XYZ. For example, the AB Doradus moving group and the Pleiades cluster have very similar velocity components, so they entirely overlap in the UVW-space. Although there are clues that these two stellar associations may have common origin (Ortega et al., 2007), presently they are spatially separated from each other. In this work we did not investigate the distribution in the XYZ space, so it may appear that some of the moving groups listed in Table 1 should be split into independent overlapping subgroups. The complete kinematical analysis should deal with the entire 6D space UVWXYZ, which is currently far away from practical capabilities of our method. Its extension from 2D to 6D would require significant additional theory work and qualitative improvements to the computing speed.
2. The geometry of the stellar groups in the UVW-space looks quite complicated. They often do not look like compact spherical or near-spherical density concentrations. Instead of that, they often appear disproportionately elongated in one or two dimensions, and possibly even curved. In some part this may be an effect of overlapping as well, but this can also reflect some natural property coming from stellar dynamics. The wavelet analysis technique has certain difficulties with processing such irregular patterns. Because of a simplified radially symmetric wavelet shape, our analysis inherently tries to decompose any elongated or membrane-like structure into a set of more or less oval-like ‘clouds’ that may need to be combined manually, e.g. as in (Ramos et al., 2018). This issue can be partly mitigated by using elliptically distorted wavelets through the use of additional scale parameters, but this would again require a drastic increase of computing time due to larger dimensions.
3. Justifying the statistical significance of the results is an important issue. We again emphasize that to correctly threshold the sample noise effect, we should use the extreme-value CWT distribution rather than the single-value one. The distribution of a single wavelet coefficient (a particular value of the CWT function) is only useful if we knew in advance which wavelet coefficient (at what shift-scale position) we plan to test. However, in practice we usually test blindly $\sim 10^3$ or $\sim 10^4$ of almost independent wavelet coefficients within a single CWT map. This eventually causes an effect of p-hacking, because the number of false alarms then grows proportionally, and false detections are then guaranteed even for very small p-value thresholds down to 10^{-3} - 10^{-4} . This requires to either perform a correction for multi-

ple testing, or to use some aggregate cumulative statistic, e.g. the maximum CWT value as in our algorithm, or a chi-square-like statistic as in (McEwen et al., 2004).

Acknowledgements. This work is supported by the Russian Foundation for Basic Research, grant 17-02-00542 A. The authors thank the anonymous reviewer for providing useful suggestions on this manuscript.

References

- Bajkova, A. T. and Bobylev, V. V.: 2018, *Astron. Lett.* **44**, 193
- Baluev, R. V.: 2008, *MNRAS* **385**, 1279
- Baluev, R. V.: 2009, *MNRAS* **393**, 969
- Baluev, R. V.: 2018, *Astron. & Comput.* **23**, 151
- Baluev, R. V. and Rodionov, E. I.: 2020, *Celest. Mech. Dyn. Astron.* **132**, 34
- Baluev, R. V., Rodionov, E. I., and Shaidulin, V. S.: 2020, *preprint arXiv.org:1903.10167*
- Baluev, R. V. and Shaidulin, V. S.: 2018, *Ap&SS* **363**, 192
- Barrado y Navascués, D., Stauffer, J. R., and Patten, B. M.: 1999, *ApJ* **522**, L53
- Bobylev, V. V. and Bajkova, A. T.: 2016, *Astron. Lett.* **42**, 90
- Bobylev, V. V., Bajkova, A. T., and Mylläri, A. A.: 2010, *Astron. Lett.* **36**, 27
- Cochrane, K. M. and Smith, G. H.: 2019, *PASP* **131**, 114201
- de Zeeuw, P. T., Hoogerwerf, R., de Bruijne, J. H. J., Brown, A. G. A., and Blaauw, A.: 1999, *AJ* **117**, 354
- Ducourant, C., Teixeira, R., Galli, P. A. B., Le Campion, J. F., Krone-Martins, A., Zuckerman, B., Chauvin, G., and Song, I.: 2014, *A&A* **563**, A121
- Eggen, O. J.: 1960a, *MNRAS* **120**, 540
- Eggen, O. J.: 1960b, *MNRAS* **120**, 563
- Eggen, O. J.: 1965, *Moving Groups of Stars*, University of Chicago Press, ILL USA
- Eggen, O. J.: 1996, *AJ* **112**, 1595

- Eisenbeiss, T., Ammler-von Eiff, M., Roell, T., Mugrauer, M., Adam, C., Neuhäuser, R., Schmidt, T. O. B., and Bedalov, A.: 2013, *A&A* **556**, A53
- Gagné, J., Lafrenière, D., Doyon, R., Malo, L., and Artigau, E.: 2014, *ApJ* **783**, 121
- Gagné, J., Mamajek, E. E., Malo, L., Riedel, A., Rodriguez, D., Lafrenière, D., Faherty, J. K., Roy-Loubier, O., Pueyo, L., Robin, A. C., and Doyon, R.: 2018, *ApJ* **856**, 23
- Gaia Collaboration; Brown, A. G. A., Vallenari, A., Prusti, T., de Bruijne, J. H. J., Babusiaux, C., Bailer-Jones, C. A. L., Biermann, M., Evans, D. W., et al.: 2018, *A&A* **616**, A1
- Gaia Collaboration; Katz, D., Antoja, T., Romero-Gómez, M., Drimmel, R., Reyl., C., Seabroke, G. M., Soubiran, C., Babusiaux, C., et al.: 2018, *A&A* **616**, A11
- Hunt, J. A. S. and Bovy, J.: 2018, *MNRAS* **477**, 3945
- Jilinski, E., Ortega, V. G., de la Reza, R., Drake, N. A., and Bazzanella, B.: 2009, *ApJ* **691**, 212
- Kraus, A., Shkolnik, E., Allers, K., and Liu, M.: 2014, *AJ* **147**, 146
- Lee, J. and Song, I.: 2018, *MNRAS* **475**, 2955
- Lee, J. and Song, I.: 2019, *MNRAS* **486**, 3434
- López-Santiago, J., Montes, D., Crespo-Chacón, I., and Fernández-Figueroa, M. J.: 2006, *ApJ* **643**, 1160
- Malo, L., Artigau, E., Doyon, R., Lafrenière, D., Albert, L., and Gagné, J.: 2014, *ApJ* **788**, 81
- Malo, L., Doyon, R., Lafrenière, D., Artigau, E., Gagné, J., Baron, F., and Riedel, A.: 2013, *ApJ* **762**, 88
- Mamajek, E. E.: 2015, in *Young Stars & Planets Near the Sun*, Vol. 10 of *Proc. IAU*, pp 21–26, Camb. Univ. Press, Cambridge
- McEwen, J. D., Hobson, M. P., Lasenby, A. N., and Mortlock, D. J.: 2004, *MNRAS* **359**, 1583
- Michtchenko, T. A., Lépine, J. R. D., Pérez-Villegas, A., Vieira, R. S. S., and Barros, D. A.: 2018, *ApJ* **863**, L37
- Monari, G., Famaey, B., Siebert, A., Wegg, C., and Gerhard, O.: 2019, *A&A* **626**, A41

- Montes, D., López-Santiago, J., Gálvez, M. C., Fernández-Figueroa, M. J., De Castro, E., and Cornide, M.: 2001, *MNRAS* **328**, 45
- Navarro, J. F., Helmi, A., and Freeman, K. C.: 2004, *ApJ* **601**, L43
- Ortega, V. G., Jilinski, E., Reza, R. D. L., and Bazzanella, B.: 2007, *MNRAS* **377**, 441
- Postnikova, E. S., Elsanhoury, W. H., Sariya, D. P., Chupina, N. V., Vereshchagin, S. V., and Jiang, I.-G.: 2020, *Research Astron. Astrophys.* **20**, 016
- Proctor, R. A.: 1869, *Proc. R. Soc. London* **18**, 169
- Ramos, P., Antoja, T., and Figueras, F.: 2018, *A&A* **619**, A72
- Ribas, I.: 2003, *A&A* **400**, 297
- Riedel, A. R., Blunt, S. C., Lambrides, E. L., Rice, E. L., Cruz, K. L., and Faherty, J. K.: 2017, *AJ* **153**, 95
- Romeo, A. B., Agertz, O., Moore, B., and Stadel, J.: 2008, *ApJ* **686**, 1
- Skuljan, J., Hearnshaw, J. B., and Cottrell, P. L.: 1999, *MNRAS* **308**, 731
- Süveges, M.: 2014, *MNRAS* **440**, 2099
- Torres, C., Quast, G., Melo, C., and Sterzik, M.: 2008, in B. Reipurth (ed.), *Handbook of Star Forming Regions: Volume II, The Southern Sky*, Vol. 5, pp 757–812, ASP Monograph Publ.
- van Leeuwen, F.: 2009, *A&A* **497**, 209
- Wright, J. T.: 2005, *PASP* **117**, 657

A Known moving groups

In this appendix, we provide summary of stellar moving groups discussed in the literature so far. They are given in Table 2 and Table 3. They contain the following data: velocity components UVW , the distance D , and the citation. All ranges are those taken from the papers. We notice that the Hercules stream is actually a whole standalone branch, possibly containing individual local subgroups (Monari et al., 2019). So we give only its rough UVW values in Table 2, and without distance. The Scorpii–Centauri branch is also very big and likely contains multiple stellar groups within, so we put them in a separate Table 3.

Table 2
Different known moving groups

U [km/s]	V [km/s]	W [km/s]	D [pc]	Ref.
118 Tau				
-12.8 ± 2.1	-19.1 ± 2.8	-9.2 ± 1.6	~ 102	Gagné et al. (2018)
32 Orinis (32 Ori)				
-11.8 ± 0.4	-18.5 ± 0.4	-8.9 ± 0.3	~ 97	Riedel et al. (2017)
-12.8 ± 2.2	-18.8 ± 2.2	-9.0 ± 2.0	~ 95	Gagné et al. (2018)
-11.2 ± 2.7	-19.7 ± 1.4	-9.1 ± 0.6	~ 106	Lee and Song (2019)
β Pictoris (β PMG)				
-10.1 ± 2.1	-15.9 ± 0.8	-9.2 ± 1.0	31 ± 21	Torres et al. (2008)
-10.94 ± 2.06	-16.25 ± 1.30	-9.27 ± 1.54	$9 - 73$	Malo et al. (2013)
-11.03 ± 1.38	-15.61 ± 1.72	-9.24 ± 2.50	$18 - 40$	Gagné et al. (2014)
-11.16 ± 2.06	-16.19 ± 1.32	-9.27 ± 1.35	$9 - 73$	Malo et al. (2014)
-10.522 ± 3.167	-15.964 ± 2.039	-9.2 ± 1.61	~ 18	Riedel et al. (2017)
-10.9 ± 2.2	-16.0 ± 1.2	-9.0 ± 1.0	~ 18	Gagné et al. (2018)
-10.0 ± 2.6	-16.2 ± 1.4	-8.9 ± 1.4	~ 24	Lee and Song (2019)
ϵ Chamaeleontis (ϵ CHA)				
-11.0 ± 1.2	-19.9 ± 1.2	-10.4 ± 1.6	109 ± 9	Torres et al. (2008)
-10.9 ± 0.8	-20.4 ± 1.3	-9.9 ± 1.4	~ 110	Riedel et al. (2017)
-9.9 ± 1.6	-19.3 ± 2.2	-9.7 ± 2.0	~ 102	Gagné et al. (2018)
η Chamaeleontis (η CHA)				
$-10.2 \pm 0.2^*$	-20.7 ± 0.1	-11.2 ± 0.1	$\sim 94^*$	Riedel et al. (2017)
-10.0 ± 1.6	-22.3 ± 2.8	-11.7 ± 1.8	~ 95	Gagné et al. (2018)
μ Ophiuchi / Mamajek2 (μ Oph)				
-12.5	-24.1	-4.9	~ 176	Jilinski et al. (2009)
ρ Ophiuchi (ρ Oph)				
-5.9 ± 1.3	-13.5 ± 4.7	-7.9 ± 4.3	~ 131	Gagné et al. (2018)
χ^{01} Fornacis (χ^{01} For)				
-12.29 ± 0.98	-20.95 ± 0.92	-4.9 ± 1.07	~ 99	Riedel et al. (2017)
-12.54 ± 0.96	-22.24 ± 1.41	-6.26 ± 2.21	~ 100	Gagné et al. (2018)
AB Doradus (ABDMG)				
-6.8 ± 1.3	-27.2 ± 1.2	-13.3 ± 1.6	34 ± 26	Torres et al. (2008)
-7.12 ± 1.39	-27.31 ± 1.31	-13.81 ± 2.16	$7 - 77$	Malo et al. (2013)
-6.96 ± 1.18	-27.23 ± 1.68	-13.90 ± 1.94	$19 - 50$	Gagné et al. (2014)
-7.11 ± 1.39	-27.21 ± 1.31	-13.82 ± 2.26	$11 - 64$	Malo et al. (2014)
-7.031 ± 2.136	-27.241 ± 1.929	-13.983 ± 1.859	~ 18	Riedel et al. (2017)
-7.2 ± 1.4	-27.6 ± 1.0	-14.2 ± 1.8	~ 14	Gagné et al. (2018)
-7.3 ± 4.6	-27.4 ± 2.6	-13.6 ± 1.9	~ 22	Lee and Song (2019)
Arcturus				
$\sim 0 \pm 50$	$\sim -120 \pm 20$	$\sim 0 \pm 25$		Navarro et al. (2004)

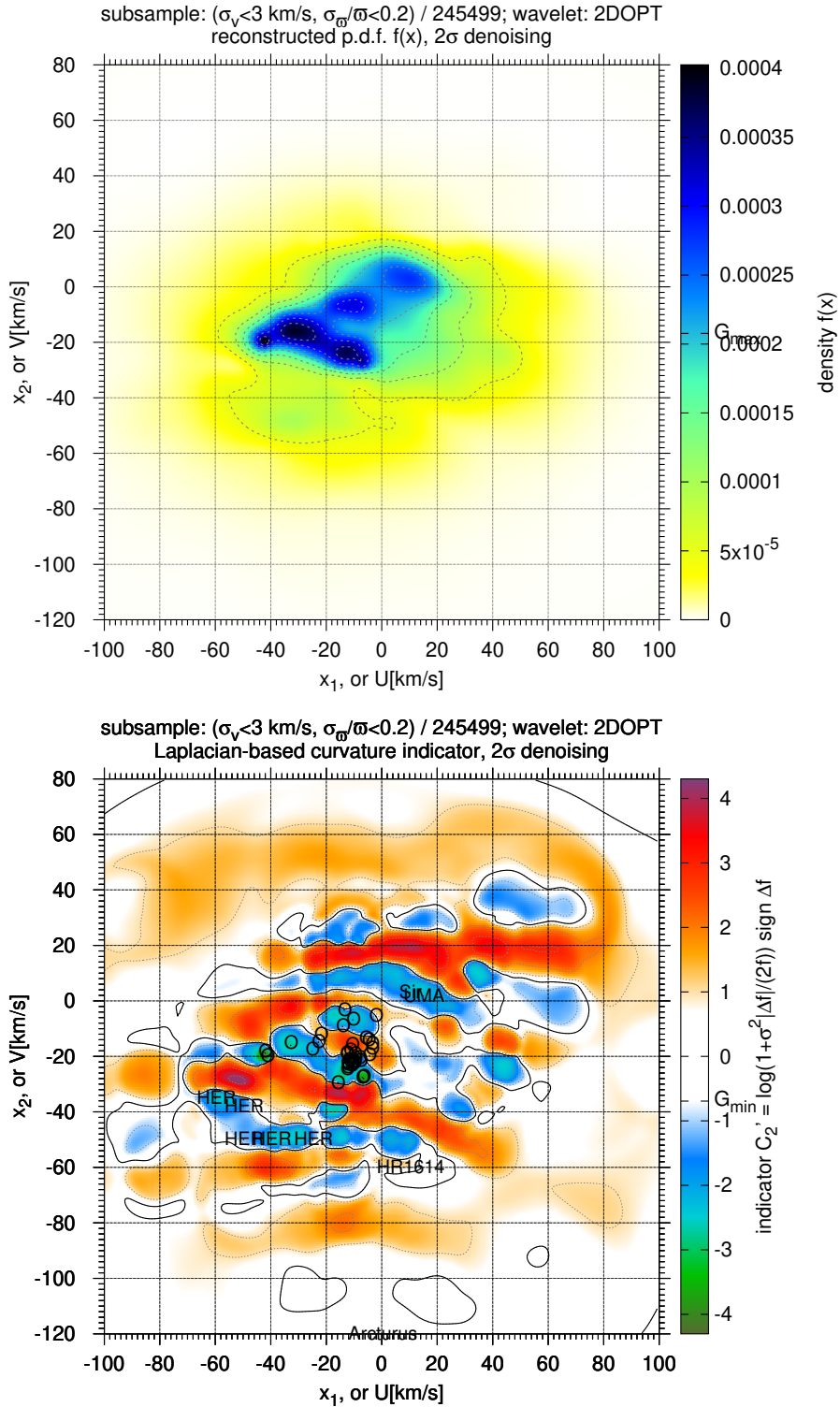


Fig. 4. Bivariate (U, V) -PDF constructed by the 2D wavelet analysis for the larger sample ($\sigma_v < 3$ km s $^{-1}$), and its Laplacian. Levels G_{\max} in PDF and G_{\min} in the Laplacian correspond to the maximum of $f(x)$ for a radially-symmetric 2D Gaussian with the same cumulative variance σ^2 . Anything above G_{\max} (below G_{\min}) is more peaky than this Gaussian. The coloring of the Laplacian map starts at $\pm|G_{\min}|$, and solid level curves follow $\Delta f \equiv 0$. Known moving groups are also plotted as text labels or O-circles.

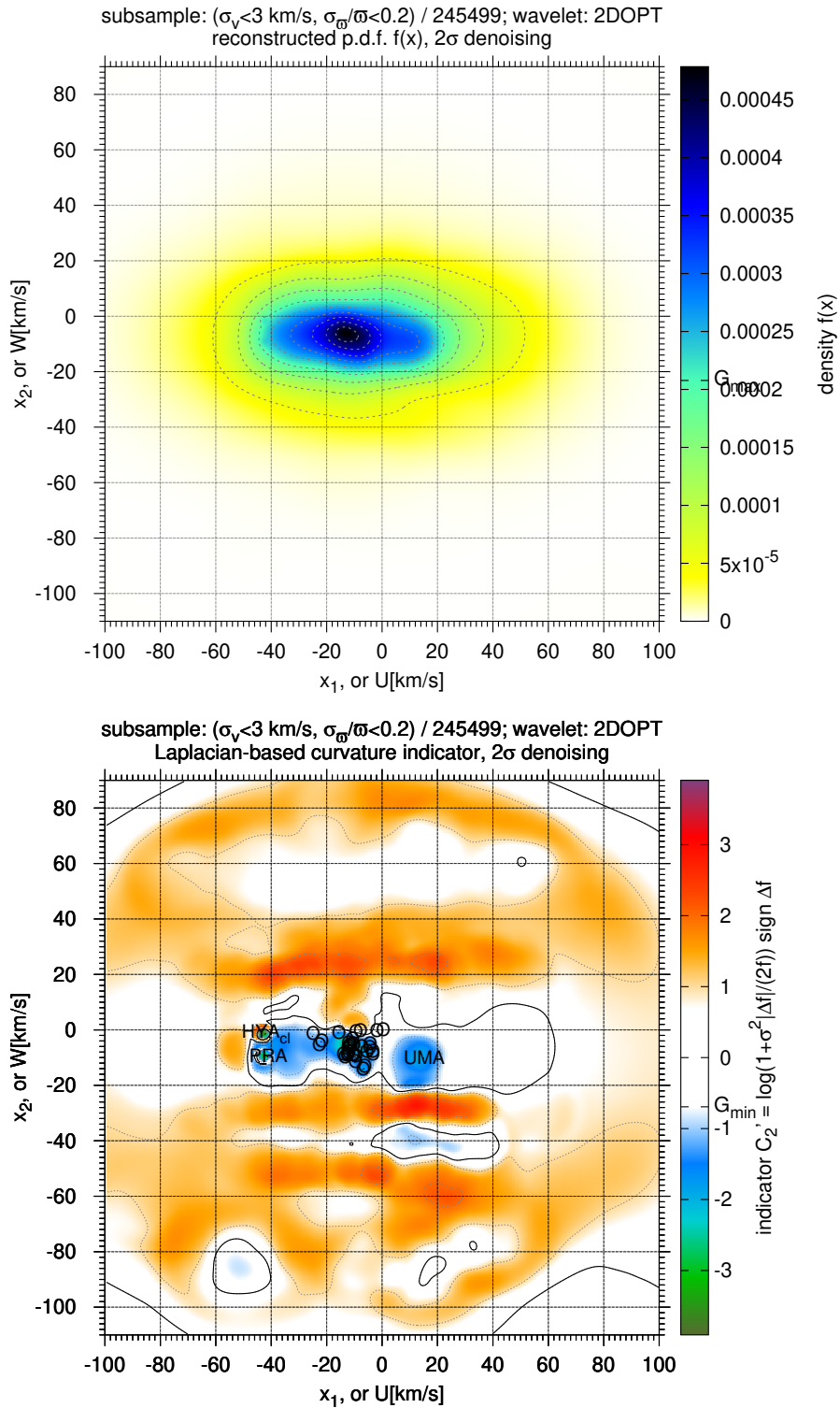


Fig. 5. Same as Fig. 4 but for (U, W) variables.

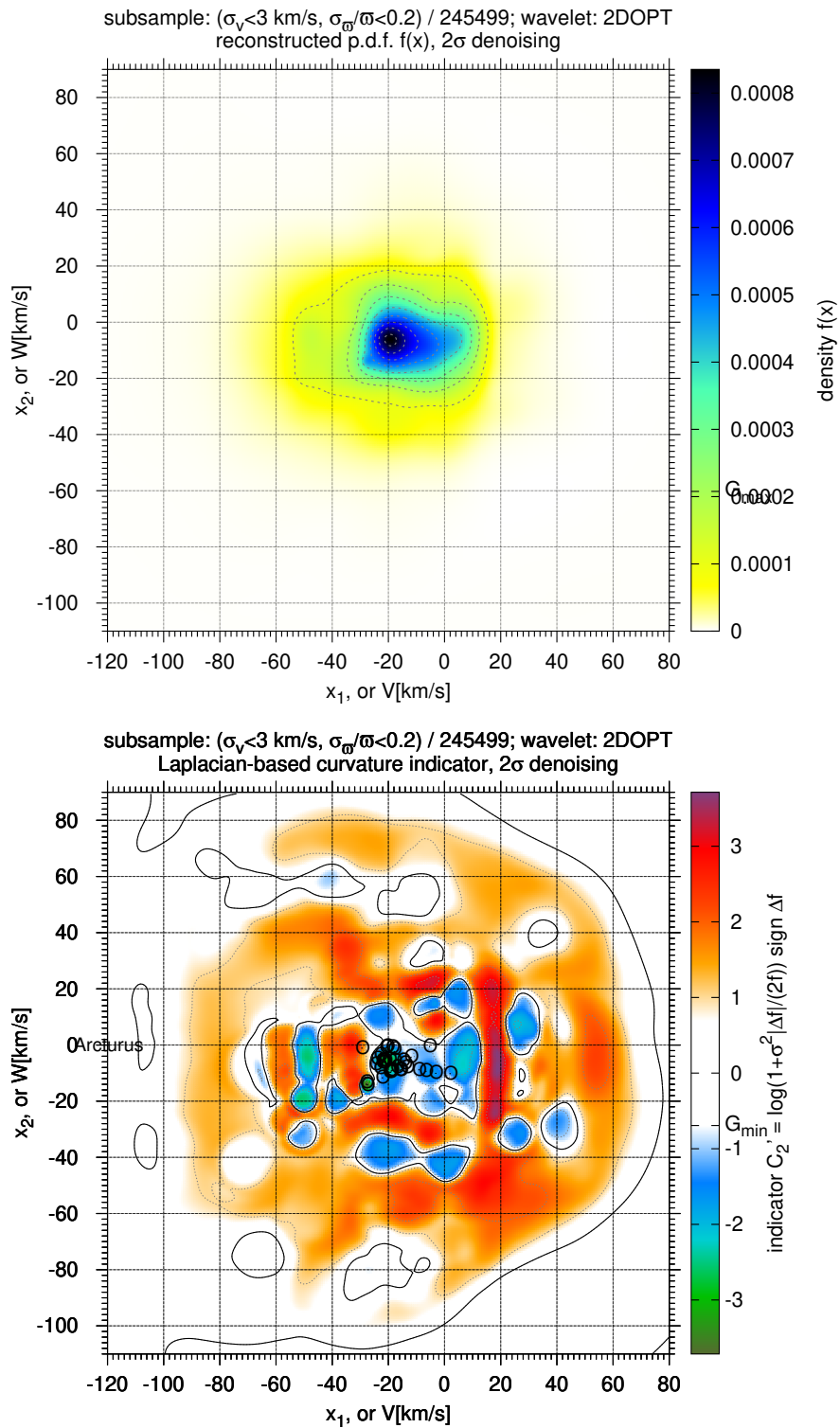


Fig. 6. Same as Fig. 4 but for (V, W) variables.

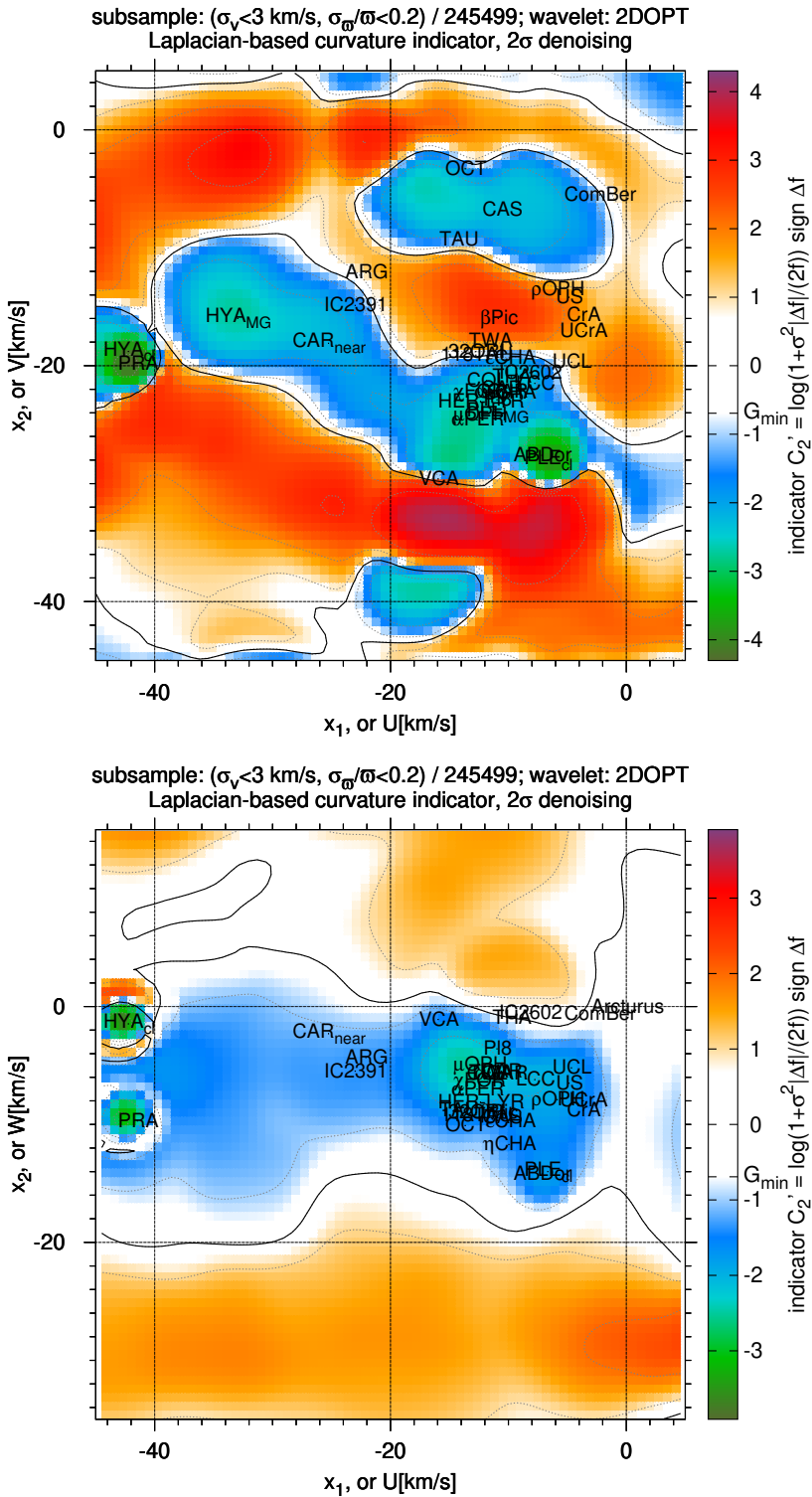


Fig. 7. Central parts of Fig. 4 and Fig. 5 expanded.

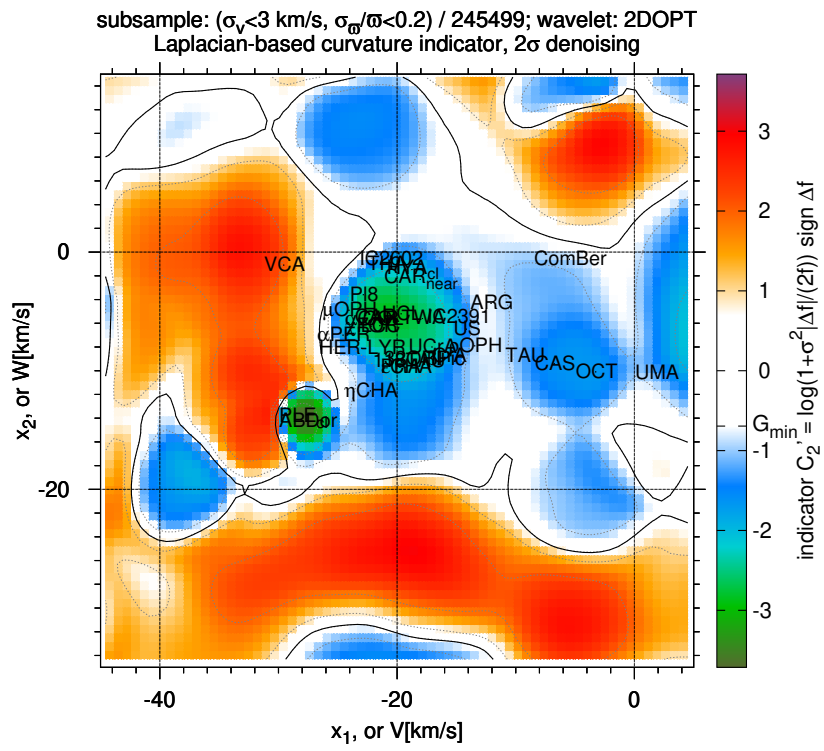


Fig. 8. Central part of Fig. 6 expanded.

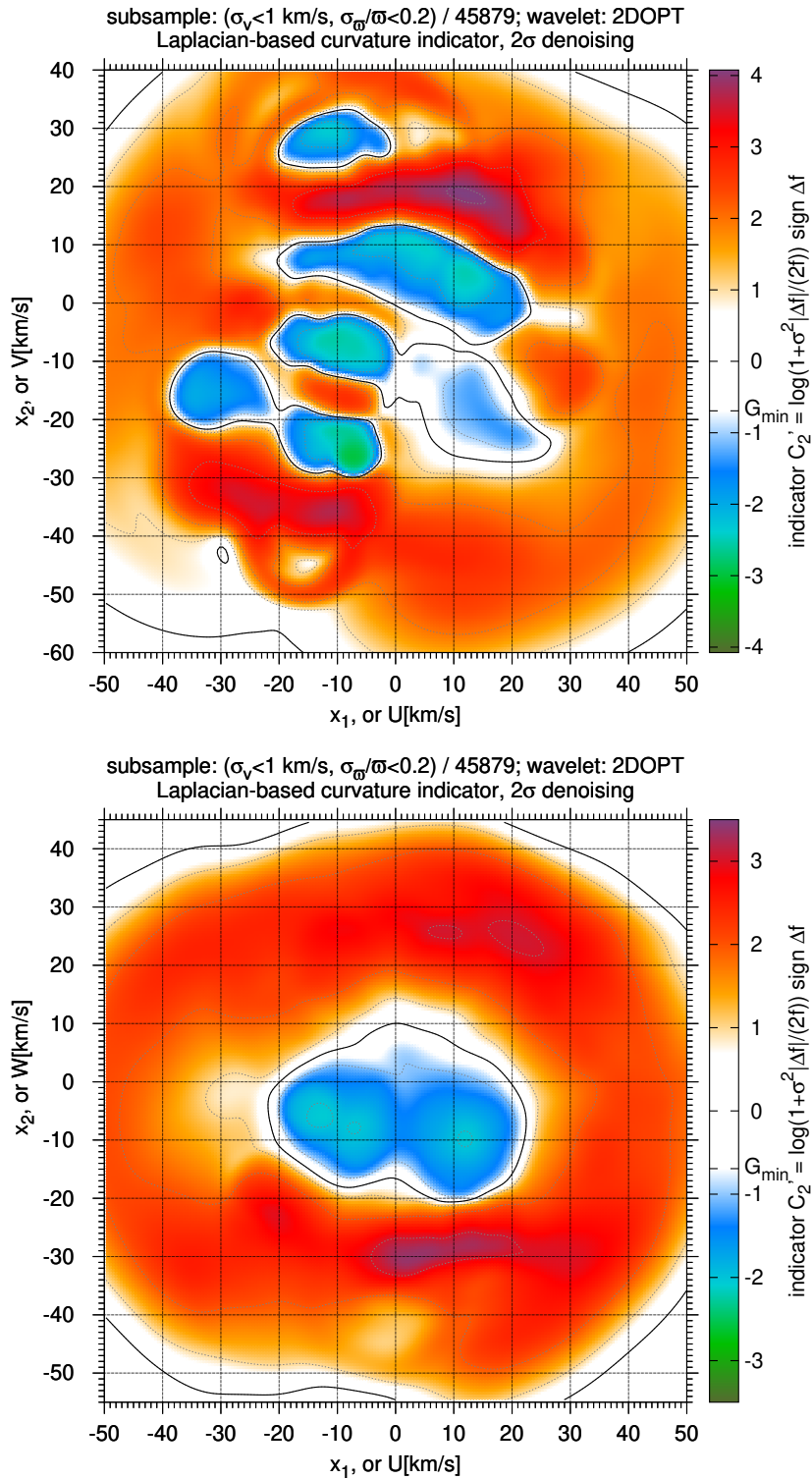


Fig. 9. Laplacians of the (U, V) and (U, W) PDFs reconstructed by 2D wavelet analysis for the smaller sample ($\sigma_v < 1 \text{ km s}^{-1}$). See also notes from Fig. 4. PDFs themselves are omitted, as well as moving groups labels.

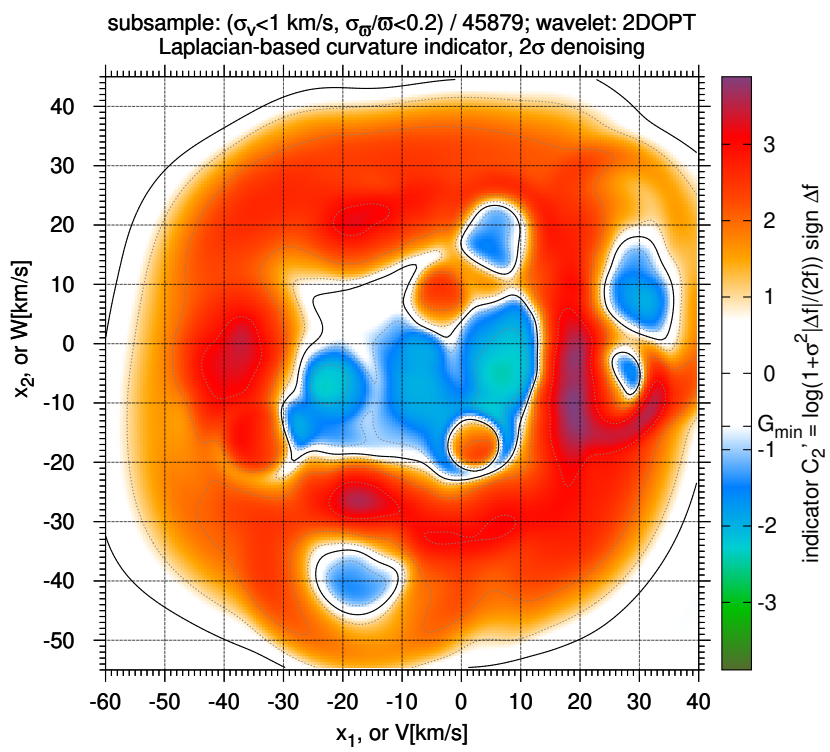


Fig. 10. Same as Fig. 9 but for the (V, W) pair.

Table 2
Different known moving groups. Continue

U, km/s	V, km/s	W, km/s	D, pc	Ref.
Argus / Carinae–Velorum (ARG)				
-22.0 ± 0.3	-14.4 ± 1.3	-5.0 ± 1.3	106 ± 51	Torres et al. (2008)
-21.78 ± 1.32	-12.08 ± 1.97	-4.52 ± 0.50	8 – 68	Malo et al. (2013)
-21.54 ± 0.87	-12.24 ± 1.67	-4.63 ± 2.74	15 – 48	Gagné et al. (2014)
-21.78 ± 1.32	-12.08 ± 1.97	-4.52 ± 0.50	8 – 68	Malo et al. (2014)
-22.133 ± 1.992	-12.122 ± 1.755	-4.324 ± 0.774	~ 27	Riedel et al. (2017)
-23.4 ± 4.9	-14.0 ± 2.6	-4.9 ± 1.7	~ 80	Lee and Song (2019)
Carinae (CAR)				
-10.2 ± 0.4	-23.0 ± 0.8	-4.4 ± 1.5	85 ± 35	Torres et al. (2008)
-10.50 ± 0.99	-22.36 ± 0.55	-5.84 ± 0.14	46 – 88	Malo et al. (2013)
-10.50 ± 0.99	-22.36 ± 0.55	-5.84 ± 0.14	46 – 88	Malo et al. (2014)
-10.691 ± 1.763	-22.582 ± 0.532	-5.746 ± 0.178	~ 72	Riedel et al. (2017)
-10.66 ± 0.67	-21.92 ± 1.02	-5.48 ± 1.01	~ 53	Gagné et al. (2018)
-10.6 ± 1.5	-22.5 ± 1.2	-4.0 ± 0.9	~ 117	Lee and Song (2019)
Carinae–Near				
-27.020 ± 3.044	-18.255 ± 1.819	-3.021 ± 1.147	~ 20	Riedel et al. (2017)
-25.3 ± 3.2	-18.1 ± 1.9	-2.3 ± 2.0	~ 28	Gagné et al. (2018)
Castor (CAS)				
-10.7	-8	-9.7	< 45	Montes et al. (2001)
-10.6 ± 3.7	-6.8 ± 2.3	-9.4 ± 2.1	$\sim 20 - 50$	Ribas (2003)
Columbae (COL)				
-13.2 ± 1.3	-21.8 ± 0.8	-5.9 ± 1.2	82 ± 30	Torres et al. (2008)
-12.24 ± 1.03	-21.32 ± 1.18	-5.58 ± 0.89	35 – 81	Malo et al. (2013)
-12.14 ± 0.51	-21.29 ± 1.27	-5.61 ± 1.69	26 – 63	Gagné et al. (2014)
-12.24 ± 1.08	-21.27 ± 1.22	-5.56 ± 0.94	35 – 81	Malo et al. (2014)
-12.311 ± 2.321	-21.681 ± 1.43	-5.694 ± 1.322	~ 49	Riedel et al. (2017)
-11.90 ± 1.04	-21.28 ± 1.29	-5.66 ± 0.75	~ 42	Gagné et al. (2018)
-12.9 ± 2.1	-21.5 ± 1.2	-5.0 ± 1.1	~ 75	Lee and Song (2019)
Comae Berenices (Coma Ber)				
-2.512 ± 1.868	-5.417 ± 1.364	-1.204 ± 1.876	~ 88	Riedel et al. (2017)
-2.30 ± 0.53	-5.51 ± 0.44	-0.61 ± 0.71	~ 85	Gagné et al. (2018)
Coronae Australis (CRA)				
-3.7 ± 1.3	-15.7 ± 2.2	-8.8 ± 2.2	~ 140	Gagné et al. (2018)
Herculis (Her)				
~ -25	~ -50			Monari et al. (2019), end of ridge
~ -40	~ -50			Hunt and Bovy (2018)
~ -50	~ -38			Gaia Collaboration; Katz et al. (2018), 1st branch
~ -50	~ -50			Gaia Collaboration; Katz et al. (2018), 2nd branch
~ -60	~ -35			Skuljan et al. (1999)
Herculis–Lyrae (Her–Lyr)				
-15.4	-23.4	~ -12	25	López-Santiago et al. (2006)
-12.41 ± 3.725	-23.03 ± 3.59	-8.11 ± 3.80		Eisenbeiss et al. (2013)

Table 2
Different known moving groups. Continue

U, km/s	V, km/s	W, km/s	D, pc	Ref.
Hyades cluster (Hya)				
-41.1 ± 0.23	-19.2 ± 0.23	-1.4 ± 0.23	~ 46	Riedel et al. (2017)
-42.27 ± 2.01	-18.79 ± 0.94	-1.47 ± 1.10	~ 42	Gagné et al. (2018)
~ -42	~ -19			Gaia Collaboration; Katz et al. (2018)
Hyades moving group				
-33	-16			Gaia Collaboration; Katz et al. (2018)
IC 2391 super cluster (IC 2391)				
-20.6	-15.7	-9.1	~ 155	Barrado y Navascués et al. (1999)
-23.04 ± 1.10	-14.89 ± 3.40	-5.48 ± 0.78	~ 149	Gagné et al. (2018)
-23.63	-14.45	-5.53		Postnikova et al. (2020)
IC 2391 stream				
-21.11	-7.21	-6.65		Postnikova et al. (2020)
IC 2602				
-8.22 ± 1.18	-20.60 ± 2.61	-0.58 ± 0.65	~ 146	Gagné et al. (2018)
Octantis (OCT)				
-14.5 ± 0.9	-3.6 ± 1.6	-11.2 ± 1.4	141 ± 34	Torres et al. (2008)
-13.673 ± 1.749	-4.8 ± 1.678	-10.927 ± 1.029	~ 115	Riedel et al. (2017)
-13.7 ± 2.4	-3.3 ± 1.3	-10.1 ± 1.4	~ 114	Gagné et al. (2018)
P18				
-11.01 ± 1.15	-22.89 ± 1.96	-3.59 ± 0.74	~ 126	Gagné et al. (2018)
Pleiades cluster (Ple)				
-6.7 ± 1.7	-28.0 ± 1.8	-14.0 ± 1.2	~ 134	Gagné et al. (2018)
~ -7	~ -28			Gaia Collaboration; Katz et al. (2018)
Pleiades moving group				
-11	-24			Gaia Collaboration; Katz et al. (2018)
Praesepe cluster (PRA)				
-41.5 ± 0.9	-19.8 ± 0.5	-9.7 ± 1.1	~ 182	van Leeuwen (2009)
Sirius moving group				
10	3			Gaia Collaboration; Katz et al. (2018)
TAU				
-14.3 ± 3.1	-9.3 ± 4.5	-8.8 ± 3.4	~ 122	Gagné et al. (2018)
Tucanae–Horologii (THA)				
-9.9 ± 1.5	-20.9 ± 0.8	-1.4 ± 0.9	48 ± 7	Torres et al. (2008)
-9.88 ± 1.51	-20.70 ± 1.87	-0.90 ± 1.31	$28 - 92$	Malo et al. (2013)
-9.70 ± 1.05	-20.47 ± 1.68	-0.78 ± 2.38	$38 - 51$	Gagné et al. (2014)
-9.93 ± 1.55	-20.72 ± 1.79	-0.89 ± 1.41	$36 - 71$	Malo et al. (2014)
-10.6 ± 0.2	-21.0 ± 0.2	-2.1 ± 0.2	~ 40	Kraus et al. (2014)
-9.802 ± 4.01	-20.883 ± 2.883	-1.023 ± 1.458	~ 40	Riedel et al. (2017)
-9.79 ± 0.87	-20.94 ± 0.79	-0.99 ± 0.72	~ 42	Gagné et al. (2018)
-9.6 ± 1.7	-21.0 ± 1.1	-1.0 ± 0.6	~ 43	Lee and Song (2019)

Table 2
Different known moving groups. Continue

U [km/s]	V [km/s]	W [km/s]	D [pc]	Ref.
TW Hydrae (TWA)				
-10.5 ± 0.9	-18.0 ± 1.5	-4.9 ± 0.9	48 ± 13	Torres et al. (2008)
-9.87 ± 4.15	-18.06 ± 1.44	-4.52 ± 2.80	28–92	Malo et al. (2013)
-11.12 ± 0.90	-18.88 ± 1.56	-5.63 ± 2.78	40–62	Gagné et al. (2014)
-10.53 ± 3.50	-18.27 ± 1.17	-5.00 ± 2.15	49–92	Malo et al. (2014)
-11.7 ± 0.9	-17.3 ± 1.3	-5.0 ± 1.0	~ 61	Ducourant et al. (2014)
-10.954 ± 3.043	-18.036 ± 2.332	-4.846 ± 1.703	~ 58	Riedel et al. (2017)
-11.6 ± 1.8	-17.9 ± 1.8	-5.6 ± 1.6	~ 55	Gagné et al. (2018)
-12.2 ± 2.6	-18.7 ± 1.2	-6.0 ± 0.9	~ 56	Lee and Song (2019)
Upper Coronae Australis (UCRA)				
-3.7 ± 3.0	-17.1 ± 1.8	-8.0 ± 1.2	~ 147	Gagné et al. (2018)
Ursa Majoris (UMA)				
14.278 ± 2.64	2.392 ± 0.594	-8.987 ± 0.407	~ 25	Riedel et al. (2017)
14.8 ± 1.0	1.8 ± 1.2	-10.2 ± 2.6	~ 25	Gagné et al. (2018)
Volantis–Carinae (VCA)				
-16.0 ± 5.4	-29.6 ± 0.9	-1.1 ± 0.6	~ 87	Lee and Song (2019)

Table 3
Scorpii–Centauri moving groups

U, km/s	V, km/s	W, km/s	D, pc	Ref.
α Persei cluster (α Per)				
–11	–26	–7	176	de Zeeuw et al. (1999)
-12.7 ± 0.9	-24.6 ± 0.7	-7.0 ± 0.2	~ 173	van Leeuwen (2009)
Cas-Tau				
–13	–20	–6	140	de Zeeuw et al. (1999)
Cep OB2				
7	2	–1	657	de Zeeuw et al. (1999)
Cep OB6				
–14	–29	–6	243	de Zeeuw et al. (1999)
Col 121				
–13	–4	–4	546	de Zeeuw et al. (1999)
Lac OB1				
5	–7	–4	373	de Zeeuw et al. (1999)
Lower Centauri–Crucis (LCC)				
–12	–13	–7	118	de Zeeuw et al. (1999)
-7.8 ± 2.7	-21.5 ± 3.8	-6.2 ± 1.8	~ 109	Gagné et al. (2018)
Per OB2				
1	–11	–1	310	de Zeeuw et al. (1999)
Tr 10				
–24	–24	–8	362	de Zeeuw et al. (1999)
Upper Centauri–Lupi (UCL)				
–9	–17	–6	140	de Zeeuw et al. (1999)
-4.7 ± 3.8	-19.7 ± 3.0	-5.2 ± 1.7	~ 126	Gagné et al. (2018)
Upper Scorpii (US)				
–1	–16	–5	145	de Zeeuw et al. (1999)
-4.9 ± 3.7	-14.2 ± 3.2	-6.5 ± 2.3	~ 132	Gagné et al. (2018)
Vel OB2				
–16	6	–1	415	de Zeeuw et al. (1999)